ACS APPLIED MATERIALS & INTERFACES

Research Article

www.acsami.org

Sub-micrometer Novolac-Derived Carbon Beads for High Performance Supercapacitors and Redox Electrolyte Energy Storage

Benjamin Krüner,[†,‡] Juhan Lee,[†,‡] Nicolas Jäckel,[†,‡] Aura Tolosa,[†,‡] and Volker Presser*[,†,‡]

[†]INM—Leibniz Institute for New Materials, 66123 Saarbrücken, Germany

[‡]Department of Materials Science and Engineering, Saarland University, 66123 Saarbrücken, Germany

Supporting Information

ABSTRACT: Carbon beads with sub-micrometer diameter were produced with a self-emulsifying novolac−ethanol−water system. A physical activation with CO_2 was carried out to create a high microporosity with a specific surface area varying from 771 (DFT) to 2237 m^2/g (DFT) and a total pore volume from 0.28 to 1.71 cm^3/g. The carbon particles conserve their spherical shape after the thermal treatments. The controllable porosity of the carbon spheres is attractive for the application in electrochemical double layer capacitors. The electrochemical characterization was carried out in aqueous 1 M Na_2SO_4 (127 F/g) and organic 1 M tetraethylammonium tetrafluoroborate in propylene carbonate (123 F/g). Furthermore, an aqueous redox electrolyte (6 M KI) was tested with the highly porous carbon and a specific energy of 33 W·h/kg (equivalent to 493 F/g) was obtained. In addition to a high specific capacitance, the carbon beads also provide an excellent rate performance at high current and potential in all tested electrolytes, which leads to a high specific power (>11 kW/kg) with an electrode thickness of ca. 200 μm.

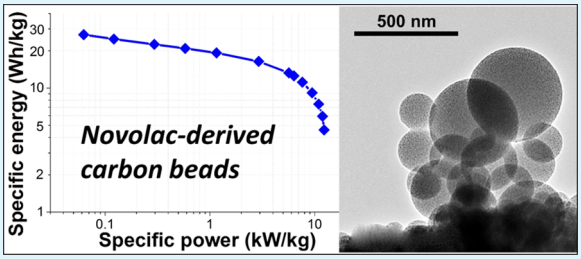

KEYWORDS: *supercapacitors, porous carbon, energy storage, redox electrolyte, self-emulsifying*

1. INTRODUCTION

Electrical double layer capacitors, also known as supercapacitors or ultracapacitors, store electrical energy via fast ion electrosorption processes at the fluid−solid interface between a charged electrode and electrolyte.[1] Due to the nonfaradaic and interfacial nature of this process, a supercapacitor typically shows a power handling ability superior to lithium ion batteries where the ions intercalate into a solid material with a suitable (often layered) structure.[2] In consequence, supercapacitors have higher specific power (800−2000 W/kg) than lithium ion batteries (typical specific power, 100 W/kg).[3] Another advantage of supercapacitors is their long cycling performance stability and high Coulombic efficiency. However, this comes at the price of a comparably low specific energy of 5−15 W·h/kg for supercapacitor cells (lithium ion batteries, ca. 100 W·h/kg).[3]

Commonly, electrodes for supercapacitor applications employ micrometer-sized particles of nanoporous carbon consolidated by the use of polymer binder.[4,5] To further enhance the power performance via fast ion transport, sub-micrometer particles are of high interest.[6−9] For example, using an emulsion synthesis process, we have recently shown the superior rate handling ability of sub-micrometer carbide-derived carbon (CDC) beads with diameters ranging from 20 to 200 nm.[10] This aligns with the enhanced performance of nanometer-sized TiC powders, which demonstrate an enhanced power rating compared to their micrometer-sized counterparts.[8] Yet, the necessity of chlorine gas to etch all noncarbon atoms makes the production of CDCs less attractive to large scale industrial processing. Also alternative synthesis methods for sub-micrometer-sized carbon particles (especially spherical ones) have been reported, such as camphoric carbon nanobeads (ca. 80 m^2/g specific surface area (SSA))[11] or spongy carbon nanobeads (16 m^2/g SSA),[12] but commonly high porosity values cannot be achieved without postsynthesis activation.

A well-established method to synthesize spherical particles (including sub-micrometer diameter) is emulsion polymerization.[13] The advantages of particle synthesis from emulsions are (i) the simplicity of the setup and scalability, (ii) the possibility to prepare a great variety of materials with a broad range in particle sizes, and (iii) a flexibility on adjusting the composition.[14] The diameters of the emulsion's liquid droplets may range from 10 nm to 100 μm, and phenolic resins can be used as carbon precursor for emulsion polymerization.[15−19] Phenolic resin systems are formed with a base or acid catalyst to obtain resoles or novolacs.[20] Resoles can cross-link without the help of cross-linking agents in contrast to novolacs which can only cross-link by adding a hardener (e.g., hexamethylenetetramine).[20] As reported in the literature so far, as-pyrolyzed beads from phenolic resin may exhibit a specific BET surface area (SSA_{BET}) up to 1131 m^2/g which can be further increased by physical or chemical activation.[17,21] Typical SSA_{BET}, which can be obtained with physical or chemical activations of carbon materials, are between 500 and 3100 m^2/g.[16,22,23] For example, the physical activation of carbon microspheres (200−1000 μm)

Received: January 18, 2016
Accepted: March 21, 2016
Published: March 21, 2016

DOI: 10.1021/acsami.6b00669
ACS Appl. Mater. Interfaces 2016, 8, 9104−9115

with CO_2 gas has been investigated by Singh and Lal, varying the CO_2 flow rate, the gasification temperature, and the activation time.[16] An increased flow rate decreased the porosity because of a shorter dwell time, while increasing the temperature from 850 to 1150 °C led to an enhanced SSA_{BET} of up to 1031 m^2/g while sacrificing the total yield of the final product.[16] A prolonged activation time from 5 to 15 h at 950 °C was the most effective step to increase the porosity: the burnoff increased from 32 to 88 mass% while the SSA_{BET} increased from 574 to 3101 m^2/g.[16]

To establish industrial production, Tennison (MAST Carbon) developed the synthesis of nonspherical phenolic-resin-derived carbon particles with a particle size of 1−50 μm.[24] By using physical activation with carbon dioxide, it was possible to achieve SSA_{BET} from 800 to 1500 m^2/g.[24] Later, Tennison et al. improved the synthesis procedure to obtain phenolic-resin-derived carbon with adjusted particle sizes between 5 and 2000 μm by using a water-in-oil emulsion.[25] Using this approach, they reached a SSA_{BET} of up to 750 m^2/g with total pore volume of ca. 1 cm^3/g. The unique feature of their synthesis is the use of pore formers, such as diols, diol-ethers, cyclic esters, cyclic and linear amides, or aminoalcohols. These pore formers do not react with the polymer but remain within the cross-linked resin and can be removed in a later stage. An initial study of the electrochemical properties of such novolac-derived carbon microbeads was provided by Fernández et al.[26] These beads were pyrolyzed at 800 °C and activated with carbon dioxide at 900 °C to obtain a SSA_{BET} up to 1773 m^2/g and up to 124 F/g capacitance in 1 M TEA-BF_4 in acetonitrile (ACN).

To overcome the inherently limited specific energy of electrical double layer capacitor, the use of redox-active electrolytes has emerged as a facile and powerful approach.[27−29] Unlike supercapacitors, redox electrolytes do not limit the energy storage capacity of the system to ion electrosorption at the fluid/solid interface at the electrode. Instead, the electrolyte volume actively participates in the energy storage mechanisms through soluble redox couples, for instance, quinone/hydroquinone, iodine/iodide/triodide, ferricyanide/ferrocyanide, or vanadium oxide.[30,31] Redox electrolyte systems provide not only a very high specific energy (10−50 W·h/kg) but also high specific power almost close to that of supercapacitors.[32] The latter can be explained by the enhanced diffusion kinetic of the redox ions in the carbon nanopores where the pore size is smaller than the equivalent diffusion layer thickness.[32] Thus, an electrode should exhibit a synergistic combination of larger transport pores for the transport of redox ions and a total high pore volume to provide a large reservoir of redox-active species. This requirement can be met with nanoporous carbon spheres with sub-micrometer size, where the large intraparticle pore volume serves as reservoir, short diffusion path lengths are provided via the small particle size, and an additional reservoir for ions is provided by large interparticle porosity.

Our work presents the synthesis of sub-micrometer novolac-derived carbon (abbreviated as NovoCarb or PNC) beads by a simple emulsion polymerization, followed by carbonization and physical activation. The self-emulsifying characteristic of the emulsion (novolac−ethanol−water) makes this synthesis method particularly practical because no high shear mixer or ultrasonic device is needed. This and the small particle size set our synthesis apart from established approaches, such as that developed by Tennison.[25] For the highly nanoporous NovoCarb spheres, we first establish the performance as a conventional supercapacitor electrode in aqueous (1 M Na_2SO_4) and organic media (1 M TEA-BF_4 in propylene carbonate, PC). Finally, the very high energy storage capacity of the material is demonstrated for aqueous 6 M KI (potassium iodide). Such a high molar concentration of potassium iodide has not been studied before, and we benchmark all data vs conventional activated carbon (AC, YP-80F from Kuraray).

2. EXPERIMENTAL DESCRIPTION

2.1. Synthesis of Ultrasmall Novolac-Derived Carbon Beads. A 25 g amount of novolac (ALNOVOL PN320, Allnex Germany GmbH) was dissolved in 100 mL of ethanol. The cross-linker, 2.5 g of hexamethylenetetramine (TCI Deutschland GmbH), was dissolved in 500 mL of Milli-Q water. The novolac−ethanol solution was added to the aqueous phase in a 1 L autoclave. The transparent solutions became milky directly after the addition of the second phase, and the self-emulsifying effect of the system eliminated the need for additional stirring of the emulsion. A pressure of approximately 3×10^6 Pa of nitrogen was applied to the autoclave before heating. The autoclave was heated to 150 °C (measured inside the autoclave) with a heating rate of 5 °C/min and held at this temperature for 8 h. The pressure increased from 3×10^6 Pa to approximately 4.3×10^6 Pa during the reaction. After synthesis, the suspension was freeze-dried using liquid nitrogen to minimize agglomeration so that a dry powder was obtained.

The novolac beads were pyrolyzed at 700 °C with a heating rate of 20 °C/min in argon (purity, 4.6) and held at this temperature for 2 h. Subsequently, physical activation via CO_2 treatment (purity of CO_2, 4.5) was carried out by heating to 1000 °C with a heating rate of 20 °C/min while CO_2 flow rate was controlled to 100 cm^3/min at 1000 °C. The process time (denoted as X; see Supporting Information Figure S1) was varied between 0 and 3 h to adjust the porosity of the carbon beads. In this work, the activation time is reflected by the subscript in the sample's name; for example, PNC_{2h} refers to phenol novolac carbon (PNC = NovoCarb) that has been exposed to 2 h of CO_2 activation.

2.2. Materials Characterization. The carbon beads were imaged by a field emission scanning electron microscope (SEM; JEOL-JSM-7500F from JEOL Ltd.) and a transmission electron microscope (TEM; JEOL JEM-2100F operating at 200 kV). The bead diameter was measured on the basis of the SEM images with ImageJ 1.47t for a number of 150 beads.[33] Chemical characterization via CHNS analysis was carried out with the Vario Micro Cube of Elementar GmbH with a temperature of the reduction tube of 850 and 1150 °C of the combustion tube. The device was calibrated with sulfanilamide.

Raman spectra were measured with a Renishaw inVia Raman Microscope, equipped with a grating of 2400 lines/mm and a 50× objective (numeric aperture, 0.9), reaching a spectral resolution of ~1.2 cm^{-1}. An Nd:YAG laser with an excitation wavelength of 532 nm was used. The acquisition time was 20−30 s, and 3−10 accumulations were used to enhance the signal-to-noise ratio. After the background noise was subtracted from the obtained Raman spectra, the D- and G-peaks were fitted with a Voigt function, as was the background contribution.

The nitrogen and carbon dioxide gas sorption analyses were carried out with a Quantachrome Autosorb iQ system. The pyrolyzed and activated samples were degassed at 150 °C for 1 h and subsequently heated to 300 °C and kept at this temperature for up to 20 h at a relative pressure of 0.1 Pa to remove volatile molecules from the surface. The nitrogen sorption analysis was performed in liquid nitrogen at −196 °C and the carbon dioxide sorption analysis at 0 °C using ethylene glycol as cooling agent. The relative pressure with nitrogen was 5×10^{-7} to 1.0 in 76 steps and 4.5×10^{-4} to 1×10^{-2} in 55 steps for the CO_2 measurements. The pore size distribution (PSD) was derived using the quenched-solid density functional theory (QSDFT), assuming slit-like pores, for the nitrogen measurements and the nonlocal density functional theory (NLDFT) for the carbon dioxide measurements.[34−36] The specific surface area (SSA) was also calculated using the Brunauer−Emmett−Teller equation (BET) in the

DOI: 10.1021/acsami.6b00669
ACS Appl. Mater. Interfaces 2016, 8, 9104−9115

linear regime of the measured isotherms, typically 3×10^{-2} to 2×10^{-1} (relative pressure), with a Quantachrome Autosorb 6B.[37] All calculations were performed with the ASiQwin-software 3.0, and the average pore size was calculated by volume weighing (i.e., d_{50} value = cumulative pore size corresponding with half of the total pore volume).[38]

The novolac beads were pyrolyzed in an Ar atmosphere (purity, 4.6) in a thermogravimetric analysis (TGA; TG209F1 Libra from Netzsch) with a heating rate of 10 °C/min to 1100 °C. A similar experiment was performed in a CO_2 atmosphere (purity, 4.5) with the pyrolyzed sample. The pyrolysis in Ar (purity, 5.0) was also investigated in a TGA with mass spectrometer (TGA-MS; STA449F3 Jupiter and QMS 403C Aëolos from Netzsch). The density of the NovoCarb particles was measured by helium pycnometry (AccuPyc 1330 pycnometer from Micromeritics; purity, 5.0).

2.3. Electrochemical Measurements. Freestanding carbon electrodes were prepared either with NovoCarb beads or commercially available activated carbon (AC, YP-80F from Kuraray) by applying polytetrafluoroethylene (PTFE; 60 mass % in H_2O) as binder. After dispersing the carbon material in ethanol, the PTFE solution was added. Then, the mixture was crushed in a mortar during the evaporation of the ethanol. The doughy carbon paste was then rolled out via a rolling machine (HR01 hot rolling machine from MTI Corp.). Finally, 120−220 μm thick freestanding electrodes were produced with 5−10 mass % PTFE for the AC based electrode and 9−12 mass % for the NovoCarb beads. Afterward, the electrodes were dried in a vacuum oven at 120 °C for 48 h at 2×10^3 Pa. For the cell assembly, an electrode disc was punched out of the rolled blank with a diameter of 12 mm. The active electrode mass varied between 2 and 15 mg depending on the activation time (Supporting Information Table S1) since the particle packing and electrode thickness were kept constant.

For the organic electrolyte (1 M TEA-BF_4 in PC; BASF, battery grade) and the aqueous system (1 M Na_2SO_4 in Milli-Q water; Sigma-Aldrich), custom-built cells were assembled employing a symmetrical two-electrode setup.[39] In order to minimize the contact resistance between the cell piston made of titanium and the electrode, a carbon-coated aluminum current collector (type Zflo 2653, Coveris Advanced Coatings, Matthews, NC, USA) was placed between the electrode and the cell piston made of titanium for measurements in organic media. In aqueous media, we used a platinum current collector instead. The electrodes were separated with a glass-fiber separator with a diameter of 13 mm (GF/A, Whatman, GE Healthcare Life Science). Before the cells were filled with the organic electrolyte in an argon-filled glovebox (MBraun Labmaster 130; O_2, H_2O < 1 ppm), they were dried at 120 °C and at 2×10^3 Pa for 24 h.

For the redox electrolyte system, a custom-made cell with graphite current collectors (10 mm thickness) was used with two-electrode configuration using two symmetric electrodes with a diameter of 12 mm. A schematic drawing is provided in Supporting Information Figure S2. To prevent the possible redox shuttling of the redox ions between anode and cathode,[40] a cation exchange membrane (FKS15, FuMA-Tech; thickness, ca. 15 μm) was used as a separator. In order to provide an effective seal for the membrane, polymer gasket layers were placed between graphite current collectors and the membrane. Through the circular inner cut (1.33 cm^2) of the gaskets, the electrodes were placed between the membrane and the current collector. Before the cell assembly, the electrodes were soaked in the redox electrolyte (1 or 6 M KI) with application of vacuum (10^4 Pa) for 5 min for degassing. During the cell assembly, the electrolyte was dropped on the electrode and the empty space in the gasket inner cut was completely filled with the electrolyte as the cell was sealed afterward.

All of the electrochemical measurements were conducted with a VMP300 potentiostat/galvanostat form BioLogic. From the obtained data, the specific capacitance was calculated with eq 1 from cyclic voltammograms (CVs) and with eq 2 for data from galvanostatic cycling with potential limitation (GCPL). The calculated capacitance values in this work are always the average of two measurements with a standard deviation below 10%. To compare the capacitance of different materials, it is common to normalize the capacitance to the active mass of the electrode material.[41]

$$C_S = \frac{I(t)}{(\mathrm{d}U(t)/\mathrm{d}t)m} \tag{1}$$

where C_S is the specific capacitance per electrode; $I(t)$, the discharge current; $\mathrm{d}U(t)/\mathrm{d}t$, the scan rate; and m, the mass of carbon in the electrode.

$$C_S = \frac{4Q_{dis}}{Um} \tag{2}$$

where C_S is the specific capacitance per electrode; Q_{dis}, the charge of the discharging cycle; U, the IR-drop corrected cell voltage; and m, the mass of carbon in the electrode.

For the calculation of the specific energy (W·h/kg) of the cells with the redox electrolyte, eq 3 was applied by integrating the cell voltage with respect to the discharging time measured in GCPL mode.

$$E = \frac{i}{m_{total}} \int U \, \mathrm{d}t \tag{3}$$

where E is the specific energy of the cell; i, the constant current applied during the measurement; and m_{total}, the total mass of the two carbon electrodes of equal weight.

To determine the electrochemical stability window of KI aqueous solution with AC activated carbon and NovoCarb beads, a voltage opening test with cyclic voltammetry was initially applied to the cells at the scan rate of 1 mV/s from 0.6 to 1.4 V in intervals of 0.05 V. In order to characterize rate handling performance, CV, and GCPL were carried out in a full cell (symmetric two-electrode setup) with 1 M TEA-BF_4 in PC, 1 M Na_2SO_4, or 1 or 6 M KI.

For long-term stability testing, voltage floating was performed with a battery cycler (BAT-SMALL battery cycler from Astrol Electronic AG) with a symmetric two-electrode cell configuration. The voltage was kept at 1.2 V in aqueous and at 2.7 V in organic electrolyte for 100 h, and the specific capacity was measured every 10 h by galvanostatic cycling (aqueous, 1.2 V; organic, 2.5 V). In the case of the redox electrolyte system, a galvanostatic cycling test was carried out at 1 A/g from 0 to 1.4 V in a symmetric two-electrode configuration.

2.4. Electrochemical Dilatometry. The height change (strain) of the carbon electrodes during charging and discharging was measured with a ECD-nano dilatometer from EL-CELL. The dilatometer cell is based on a two-electrode design using an oversized PTFE-bound AC as counter and quasi-reference electrode. The investigated electrodes were compressed between the separator and a movable titanium plunger with a constant weight load of 10 N. Prior to the experiments, the cell was dried for 12 h at 120 °C under vacuum (2 kPa). A DP1S displacement transducer (Solartron Metrology), with an accuracy of 15 nm, was used. The experiments were performed at constant temperature of 25.0 ± 0.1 °C using a climate chamber (Binder). Prior to the electrochemical characterization, the cell was conditioned with a holding period at 0 V vs carbon for 10 h followed by five charge/discharge cycles between 0 and 2.5 V vs carbon, and only data of the fifth cycle are shown.

3. RESULTS AND DISCUSSION

3.1. Morphology and Porosity. Electron microscopy confirmed conservation of the spherical droplets structure generated in the emulsion after polymerization and pyrolysis (Figure 1A,B). Image analysis yielded an average number-dependent sphere diameter of 302 ± 142 nm for PNC_{0h}. Transmission electron microscopy (TEM) also showed the highly homogeneous character of the beads with no differentiation, for example, between core and shell. The overall nonordered character of the carbon is also evident from the absence of lattice fringes or visible crystalline domains (Figure 1B, inset). As seen from Figure 1C,D, the size of the particles

DOI: 10.1021/acsami.6b00669
ACS Appl. Mater. Interfaces 2016, 8, 9104−9115

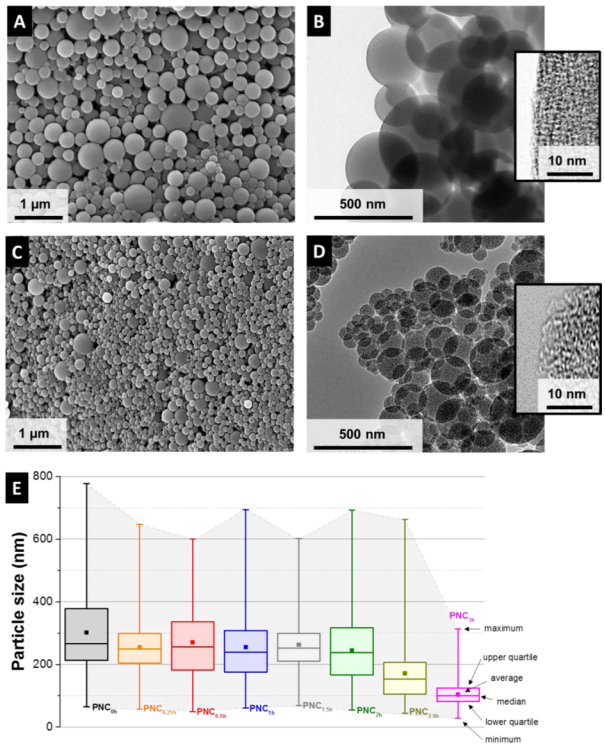

Figure 1. SEM images (A, C) and TEM images (B, D) of PNC_{0h} (A, B) and PNC_{3h} (C, D). Box–whisker plot (E) with maximum and minimum, upper and lower quartile, and number-dependent average and median of the carbon beads after the pyrolysis PNC_{0h} and after CO_2 activation ($PNC_{0.25h}$, $PNC_{0.5h}$, PNC_{1h}, $PNC_{1.5h}$, PNC_{2h}, $PNC_{2.5h}$, and PNC_{3h}).

after 3 h of CO_2 activation was significantly reduced to 104 ± 40 nm as was the spread of minimum and maximum diameters (Figure 1E and Supporting Information Figures S3 and S4). No significant change in bead diameter was encountered for CO_2 activation up to 2.5 h. The noncrystalline character of the carbon beads can be seen well from high resolution TEM micrographs (Figure 1D, inset) and the increased transparency of CO_2-treated beads indicates that the particles became less dense through removal of carbon by the physical activation (see also Supporting Information Figure S5).

To further investigate the pyrolysis process and CO_2 activation as a facile way to enhance the porosity of NovoCarb beads, we carried out thermogravimetric analysis. The TGA data presented in Figure 2A show the mass loss of the carbon beads during the pyrolysis and the CO_2 treatment. The pyrolysis of phenolic resins can be classified in three phases.[42] The small mass loss at approximately 100 °C was not part of the three stages of the pyrolysis and was caused by desorption of water and other light molecules (e.g., ethanol and ammonia; Supporting Information Figure S5). The first stage is identified by the formation of cross-links and the evolution of water and other condensates between 200 and 500 °C. The second stage is dominated by breaking cross-linking bonds between 400 and 800 °C (i.e., amino, methylene, and oxygen groups). This leads to the evolution of water, carbon monoxide, nitrogen, and amino groups among others (Supporting Information Figure S5). The oxygen signal is dropping at approximately 350 and 630 °C because of the evolution of carbon dioxide. The residual oxygen of the Ar flow is also reacting with the sample during the pyrolysis, and the final stage (560–900 °C) is dominated by the production of hydrogen by the splitting of hydrogen atoms directly bonded to benzene nuclei.[42] Pyrolyzed carbon is formed in this temperature range via the coalescence of aromatic rings, and the yield is 48 mass % at 700 °C and 43 mass % at 1100 °C of the initial sample mass. During the CO_2 treatment, we observed a massive oxidation-induced mass loss above 950 °C and adjusted the activation parameters to 1000 °C for this study.

As seen from electron micrographs, the beads became smaller and rougher with progressed activation (Figure 1C–E). With an additional decrease in contrast, TEM images indicate an increase in particle porosity, while the small nanopores themselves cannot be resolved by the imaging method directly. A more detailed characterization of the porosity of the beads prior to and after thermal activation with CO_2 for different durations can be gained by gas sorption analysis (GSA), as shown in Figure 2B–D.[38] Values for the mass loss, SSA_{BET} and SSA_{DFT}, total pore volume, and average pore size are provided in Table 1. The pyrolyzed carbon beads showed exclusively micropores with pores only smaller than 0.8 nm and a SSA_{DFT} of 771 m^2/g. The average pore size was 0.5 nm which is similar to the calculated molecular diameter of ethanol (0.52 nm),[43] indicating the role of ethanol as a pore former. The CO_2 activation and the increase in activation time led to a higher total mass loss. The SSA_{DFT} also increased to reach a maximum of 2237 m^2/g (SSA_{BET}, 3104 m^2/g) with a total pore volume of 1.71 cm^3/g at a mass loss of 90 mass %. These values are similar to the highest SSA_{BET} reported in literature for activated carbon materials.[16,22,23] Progressing activation caused a coalescence of the pores and a progressing increase of the average pore size. Finally, the enhanced pore coalescence at an activation of more than 2 h led to an ultimate decrease of the SSA and total pore volume while the average pore size constantly increased (Figure 2B). Additionally, the width of the pore size dispersity increased from 0.3 to 1.1 nm (PNC_{0h}) to 0.4–2.0 nm (PNC_{1h}) and to 0.5–3.4 nm (PNC_{3h}).

3.2. Structure, Density, and Chemical Composition.

TEM micrographs (Figure 1) evidenced the amorphous nature of NovoCarb beads and the lack of crystalline ordering after pyrolysis and CO_2 activation. Further insights into the carbon structure can be gained by means of Raman spectroscopy (Table 2). The Raman spectrum of PNC_{0h} is shown in Figure S6A (Supporting Information) with the fitted peaks for D-mode (at 1345 cm^{-1}) and G-mode (at 1602 cm^{-1}). The I_D/I_G ratio can be used to calculate the average in-plane domain size (L_a),[44] for example with the Tuinstra–Koenig[45] or the Ferrari–Robertson equation.[46] To understand the data, we need to consider that the two equations are only valid for different domain sizes: the Tuinstra–Koenig (TK) equation can be used for L_a < 2 nm and the Ferrari–Robertson (FR) equation for L_a > 2 nm.[47] We have to assume a transition in the values from the TK to the FR model, as shown in Figure S6C. Starting from an amorphous polymeric precursor, the pyrolyzed carbon showed a relatively small L_a of 1.4 nm. This value slightly increased after activation due to the longer holding time at higher temperatures and the removal of nongraphitic carbon for $PNC_{0.25h}$ (1.5 nm) and $PNC_{0.5h}$ (1.7 nm). For longer activation durations and L_a close to the critical domain size of 2 nm, we have to transition to the use of the FR model. Accordingly, the L_a values for PNC_{1h} to PNC_{3h} showed a small level of variation between 2.3 and 2.5 nm.

The two competing effects of graphitic domain size growth at high temperatures and the removal of carbon atoms by the

DOI: 10.1021/acsami.6b00669
ACS Appl. Mater. Interfaces 2016, 8, 9104–9115

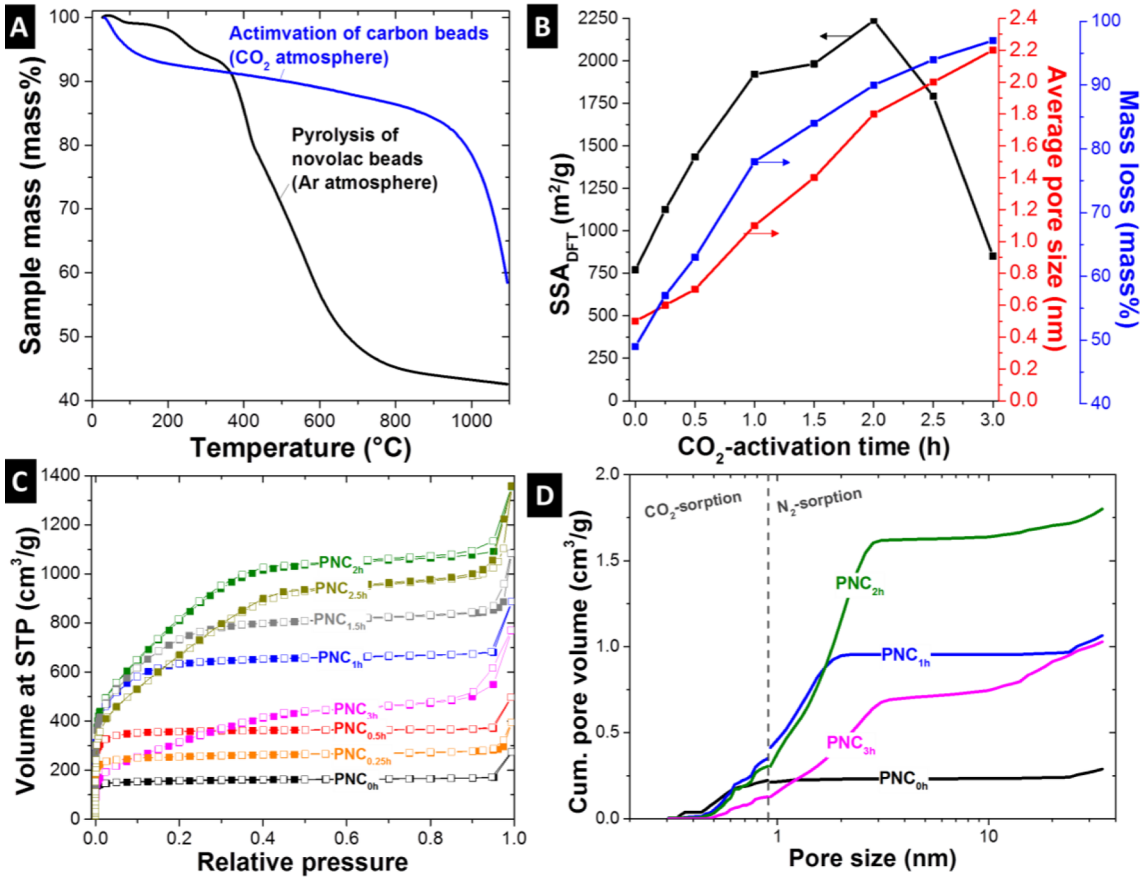

Figure 2. TGA of the pyrolysis of novolac beads in Ar atmosphere and of the CO_2 treatment of the pyrolyzed beads recorded with a heating rate of 10 °C/min (A). Correlation of SSA_{DFT}, average pore size, and mass loss on the CO_2-activation time (B). Nitrogen sorption isotherms at −196 °C on carbon beads (C). Cumulative pore size distributions of the CO_2 (at 0 °C) and N_2 (at −196 °C) gas adsorption measurement of the samples PNC_{0h}, PNC_{1h}, PNC_{2h}, and PNC_{3h} (D).

Table 1. Mass Loss of the Beads Introduced by the Pyrolysis and CO_2-Activation and Surface Characteristics of the Carbon Beads[a]

	mass loss (mass %)	SSA_{DFT} (m^2/g)	SSA_{BET} (m^2/g)	total pore vol (cm^3/g)	av pore size (nm)
PNC_{0h}	49	771	624	0.28	0.5
$PNC_{0.25h}$	57	1125	998	0.44	0.6
$PNC_{0.5h}$	63	1434	1433	0.57	0.7
PNC_{1h}	78	1921	2383	1.05	1.1
$PNC_{1.5h}$	84	1982	2633	1.32	1.4
PNC_{2h}	90	2237	3104	1.71	1.8
$PNC_{2.5h}$	94	1792	2571	1.58	2.0
PNC_{3h}	97	851	1189	0.88	2.2
AC		1756	2347	1.15	1.6

[a]For data on AC, see also ref 61.

Table 2. Peak Fitting Results of the Raman Spectra, with Position of the D- and G-Mode, the FWHM, I_D/I_G Ratio and L_a

	mode	position (cm^{-1})	FWHM (cm^{-1})	I_D/I_G	L_a (nm)
PNC_{0h}	D	1345.0	165.9	2.49	1.43
	G	1601.9	66.7		
$PNC_{0.25h}$	D	1346.2	173.5	2.32	1.55
	G	1600.8	74.7		
$PNC_{0.5h}$	D	1345.7	164.5	2.02	1.71
	G	1597.8	81.5		
PNC_{1h}	D	1339.6	132.9	2.17	2.49
	G	1601.2	61.2		
$PNC_{1.5h}$	D	1339.4	126.7	2.03	2.31
	G	1601.8	62.4		
PNC_{2h}	D	1336.2	122.9	2.07	2.39
	G	1600.9	59.4		
$PNC_{2.5h}$	D	1335.1	122.2	2.08	2.37
	G	1599.8	58.7		
PNC_{3h}	D	1335.1	122.0	2.11	2.41
	G	1599.7	57.9		

physical activation influence the domain size of the carbon materials, as also seen from Raman spectroscopy (Supporting Information Figure S6c). The position of the D-mode shifted from 1345 to 1335 cm^{-1} when increasing the activation time. For comparison, the G-mode of all samples was located at approximately 1600 cm^{-1}, which indicates partially graphitic carbon, as also supported by a range of I_D/I_G ratio between 2.02 and 2.49.[48] For the physical activation, we have to consider the preferential etching of less-ordered carbon in addition to structural ordering caused by the thermal treatment.

The analysis of the skeletal density supports the transition toward a higher degree of carbon ordering. Initially, the density of the pyrolyzed carbon beads was 1.99 ± 0.01 g/cm^3. For comparison, glassy carbon has a density of 1.48 g/cm^3 and graphite of 2.25 g/cm^3.[49] Activation led to an initial increase of the skeletal density after 1 h (2.33 ± 0.08 g/cm^3), as shown in

DOI: 10.1021/acsami.6b00669
ACS Appl. Mater. Interfaces 2016, 8, 9104−9115

Table 3. Results of the CHNS Analysis[a]

	C (mass %)	H (mass %)	N (mass %)	S (mass %)	ΔO (mass %)
ALNOVOL PN 320	73.4 ± 1.7	5.83 ± 0.27	≤0.2	b.d.	20.8 ± 1.7
polymer beads	70.8 ± 1.3	6.32 ± 2.22	2.3 ± 0.1	b.d.	20.5 ± 2.6
PNC_{0h}	92.6 ± 1.5	1.34 ± 0.02	≤0.4	b.d.	5.7 ± 1.5
$PNC_{0.25h}$	90.7 ± 2.2	1.04 ± 0.03	≤0.5	b.d.	7.8 ± 2.3
$PNC_{0.5h}$	90.4 ± 1.6	1.13 ± 0.02	≤0.4	b.d.	8.1 ± 1.6
PNC_{1h}	90.1 ± 2.8	0.82 ± 0.05	≤0.5	b.d.	8.6 ± 2.8
$PNC_{1.5h}$	90.4 ± 8.7	0.77 ± 0.04	≤0.5	b.d.	8.3 ± 8.7
PNC_{2h}	89.3 ± 2.5	0.90 ± 0.13	≤0.8	b.d.	9.0 ± 2.6
$PNC_{2.5h}$	82.1 ± 4.5	0.66 ± 0.40	≤0.7	b.d.	16.6 ± 4.6

[a]The difference to 100% is attributed to oxygen and listed as ΔO; as no other elements were seen by elemental analysis with energy-dispersive X-ray analysis (EDX), the value for ΔO is an approximation for the actual oxygen content (b.d.: below limit of detection).

Figure S7 (Supporting Information). This value is relatively high compared to other CO_2-activated resol-derived carbons in the literature (2.2 g/cm^3; see ref 24), and this can be explained with the removal of less-dense material by the CO_2 activation and enhanced structural ordering of disordered carbon at high temperature. Continued CO_2 activation decreased the density to 1.95 ± 0.07 g/cm^3 after 1.5 h and to 1.51 ± 0.05 g/cm^3 after 2 h (the latter is the sample with the highest SSA and pore volume). The measured skeletal density after 2.5 h of CO_2 treatment was the lowest, namely, 1.44 ± 0.05 g/cm^3 (sample showing an onset of decreasing SSA).

Chemically, as shown by EDX analysis exemplified for PNC_{0h}, the beads predominantly consisted of carbon with some amounts of oxygen (Supporting Information Figure S8). These data were characteristic for all samples. The much higher sensitivity and accuracy of CHNS analysis allow a more precise quantitative analysis. Since EDX did not detect other elements outside the CNHS system except oxygen, we used the latter method to also assess the oxygen content (referred to as ΔO; Table 3). Initially, the novolac beads showed a carbon content of 70.8 mass %, which increased after pyrolysis to 92.6 mass % and decreased after CO_2 activation to 90.7 to 82.1 mass % (with a major decrease of the carbon content $PNC_{2.5h}$). While, after pyrolysis, ΔO was decreased from 20.5 to 5.7 mass %, CO_2 activation led to a slight increase to 7.8−9.0 mass % (for $PNC_{0.25h}$ to PNC_{2h}). The hydrogen content decreased from 6.3 mass % of the polymer beads to a nondetectable level after pyrolysis. The nitrogen content was lowered after the pyrolysis from 2.3 mass % to only ≤0.4 mass %, yet the nitrogen content increased after the CO_2 activation to ≤0.8 mass %, which can be explained by the preferred removal of carbon (i.e., the nitrogen content only increased relatively).

3.3. Supercapacitor Performance in Aqueous and Organic Electrolytes. Electrochemical characterization (Table 4) of NovoCarb beads as supercapacitor electrodes was carried out for aqueous (1 M Na_2SO_4) and organic electrolyte media (1 M TEA-BF_4 in PC). Aqueous media are highly attractive because of the reduced energy required during supercapacitor manufacturing invested for thorough drying of the electrode materials and the low electrolyte costs.[50] Especially pH-neutral electrolytes are very promising because of their high electrochemical performance stability and beneficial voltage window.[51] Organic electrolytes are currently in widespread use for commercial supercapacitors because of their extended voltage window up to 2.7 V, although ion mobility is lower than in aqueous media.[50] The cyclic voltammograms of the carbon beads (Figure 3A,B) show that even a short physical activation (e.g., $PNC_{0.25h}$) was sufficient to

Table 4. Specific Capacitance of the Carbon Beads in Aqueous 1 M Na_2SO_4 and 1 M TEA-BF_4 in PC (n.d., Not Determined; for Comparison, Data for AC Given As Well)

	specific capacitance in aqueous 1 M Na_2SO_4 (F/g)	specific capacitance in 1 M TEA-BF_4 in PC (F/g)
AC	140	103
PNC_{0h}	n.d.	1
$PNC_{0.25h}$	84	44
$PNC_{0.5h}$	89	84
PNC_{1h}	117	112
$PNC_{1.5h}$	127	123
PNC_{2h}	123	123

enable enhanced double layer capacitance. As the only exception, the nonactivated pyrolyzed material (PNC_{0h}) did not yield stable electrochemical performance in aqueous media and was deselected for further characterization. In general, longer activation enhanced the SSA and a higher specific capacitance can be seen. The highest capacitance of 127 F/g at 1.2 V was achieved after 1.5 h of CO_2 activation, even though the highest SSA was achieved after 2 h. Obviously, limitations to the achievable specific capacitance of highly porous carbons with high surface area are encountered,[52] such as limited interfacial capacitance in carbon nanopores with very thin walls and incomplete charge screening.[53]

Like in aqueous media, the CVs showed also the behavior of a near-ideal capacitor in 1 M TEA-BF_4 in PC (Figure 3B) for an activation duration of 0.5 h or longer. A maximum of 123 F/g was measured for $PNC_{1.5h}$ and PNC_{2h} at 2.5 V. All CV were pronouncedly rectangular with a continuous increase in capacitance for higher cell voltages (known as butterfly shaped CV) stemming from electrochemical doping.[39,54] As an exception, the CV of $PNC_{0.25h}$ showed a continuous narrowing and reduced capacitance at higher voltages which was not observed in aqueous media (Figure 3A). This effect can be explained by steric (volumetric) effects as shown by Segalini et al. for nanoporous carbon with a very narrow pore size distribution and an average size of 0.68 nm (TiC-CDC) for 1 M TEA-BF_4 in ACN as electrolyte.[55] For comparison, the ionic diameters of ACN-solvated TEA^+ and BF_4^- are 1.30 and 1.16 nm, respectively, and similar values are expected for PC (1.35 nm for TEA^+ in PC and 1.40 nm for BF^{4-} in PC).[56] Ion electrosorption in pores smaller than this value is accomplished by (partial)[57] desolvation (ionic diameter, 0.67 nm for TEA^+ and 0.45 nm for BF_4^-).[58] Smaller ion diameters are expected for the aqueous media, and, thus, no such effects were seen for $PNC_{0.25h}$ in 1 M Na_2SO_4.[59] In our case, $PNC_{0.25h}$ had an average pore size of 0.6 nm which poses severe accessibility

DOI: 10.1021/acsami.6b00669
ACS Appl. Mater. Interfaces 2016, 8, 9104−9115

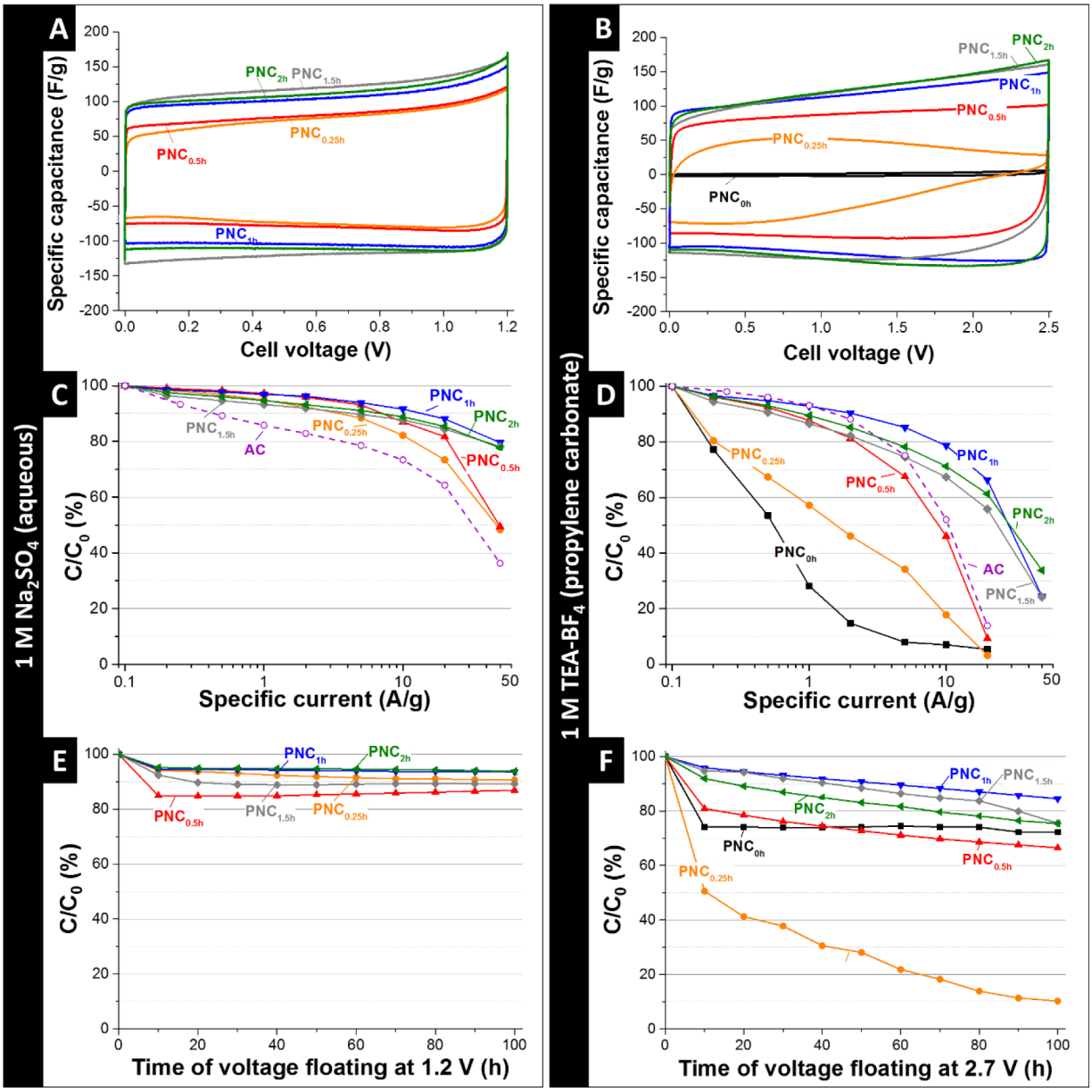

Figure 3. CVs of the carbon bead film electrodes in aqueous 1 M Na_2SO_4 (A) and in 1 M TEA-BF_4 in PC (B) with a scan rate of 5 mV/s. Rate handling of the film electrodes in aqueous 1 M Na_2SO_4 (C) and in 1 M TEA-BF_4 in PC (D) from a range of specific current of 0.1−50 A/g. For comparison, the rate handling ability of a conventional activated carbon (AC) is added as well to panels C and D. Long-time floating stability testing in aqueous 1 M Na_2SO_4 at 1.2 V (E) and in 1 M TEA-BF_4 in PC at 2.7 V (F).

limitations to the electrolyte ions in organic media (Table 1). CO_2 activation for at least 0.5 h was sufficient to yield an average pore size of 0.7 nm or more and no steric hindrance, and resulting CV deformation is observed.

In situ electrochemical dilatometry supports that $PNC_{0.5h}$ suffered from volumetric restrictions to ion electrosorption in sub-nanometer carbon micropores (Supporting Information Figure S9). In particular, we see an increased strain of $PNC_{0.25h}$ when compared to $PNC_{0.5h}$. At 75 C/g, $PNC_{0.25h}$ shows a small expansion of 0.07%, compared to 0.05% of $PNC_{0.5h}$ and the values divert at 175 C/g, namely, 0.29% and 0.22%, respectively. The ion sieving effect leads to a higher desolvation of ions to fit into the pores of $PNC_{0.25h}$ and a higher total strain of the electrode. PNC_{0h} with even smaller pores (average pore size = 0.5 nm) and moderate specific surface area (SSA_{DFT} = 771 m^2/g) yielded a negligible specific capacitance of around 1 F/g (since the ion radius of bare BF_4 is 0.45 nm) and, in comparison, a severely enhanced strain of 0.28% at 75 C/g.[58] These data align well with the increased pore swelling caused by steric effects when the pore size rivals the ion size shown by Hantel et al. for TiC-CDC in 1 M TEA-BF_4 in ACN with in situ electrochemical dilatometry.[60]

All NovoCarb samples showed an excellent rate handling ability in aqueous media with a loss of capacitance of less than 7% at 1 A/g (Figure 3C). Activation for 1 h or longer enabled one to maintain more than 77% of the initial low rate capacitance at a high specific current of 50 A/g. This high power handling ability is also reflected by the very small distortion of CVs at very high scan rates of 1 V/s, as exemplified for PNC_{2h} (Supporting Information Figure S10A). For all activation conditions in aqueous Na_2SO_4, the measured power performance was also superior compared to a conven-

DOI: 10.1021/acsami.6b00669
ACS Appl. Mater. Interfaces 2016, 8, 9104−9115

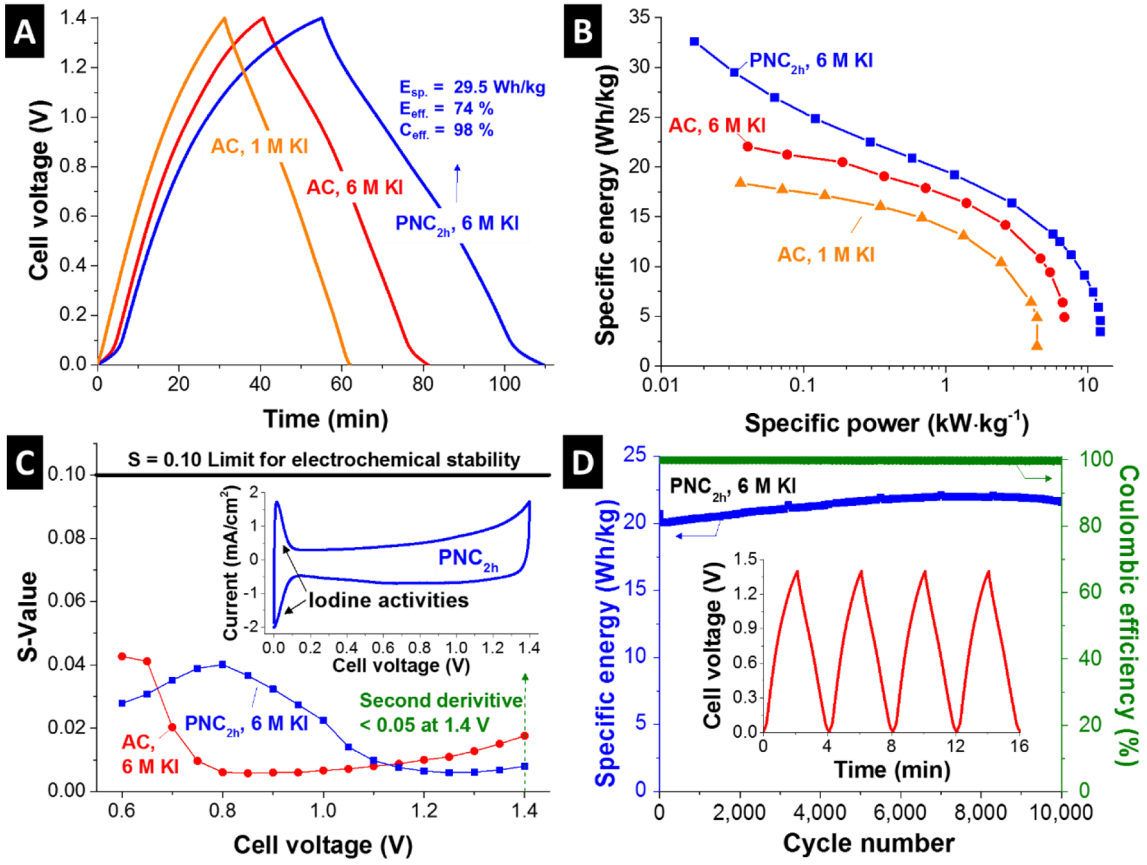

Figure 4. Galvanostatic charge/discharge curve at 50 mA/g (A) and the rate characteristics (B) obtained at various specific power in the cell voltage range from 0 to 1.4 V for different redox electrolyte systems. AC is a standard activated carbon used for the comparison of the performance for 1 and 6 M KI (aqueous). The electrochemical stability window was evaluated by the *S*-value method for 6 M KI with AC or PNC_{2h}. The inset shows the cyclic voltammogram of the cell with PNC_{2h} in 6 M KI at 1 mV/s for the cell stability window of 1.4 V. (C). Cyclic stability testing of PNC_{2h} in 6 M KI in the cell voltage range from 0 to 1.4 V at 1 A/g for 10,000 cycles and galvanostatic charge/discharge curve of the first few cycles (D).

tional nanoporous AC, for which the specific capacitance dropped to 86% at 1 A/g of the initial capacitance and to 73% at 10 A/g. In PC, a much lower overall rate handling is observed in agreement with the much lower ion mobility.[61] Perfectly aligning with the accessibility issues seen from CV and dilatometry, we see a very poor rate handling for PNC_{0h} and $PNC_{0.25h}$ (Figure 3D). On-setting for an activation time of 0.5 h (corresponding to an average pore size of 0.7 nm), we see an enhanced power performance and PNC_{1h} already significantly surpasses the values seen for the activated carbon reference. In detail, PNC_{1h} provided 78% of the initial capacitance at a very high specific current of 10 A/g compared to 52% for AC. The beneficial power handling ability of NovoCarb is also exemplified for PNC_{2h} when sweeping the scan rate in CV up to 1 V/s.

The enhanced power handling ability may relate to the sub-micrometer size of the NovoCarb beads used in this study. This aligns with the conclusions drawn by Perez et al. that nanosizing is an effective tool to enhance the rate handling ability even when comparing materials with virtually identical pore size distribution.[8] Consequently, the improved power performance of NovoCarb beads over micrometer-sized activated carbon is well-explained. When compared to spherical carbide-derived carbon with an average particle diameter of ca. 150 nm, we still see an enhanced performance of NovoCarb. In particular, the mentioned CDC beads material maintained at 20 A/g 80% of the initial low rate capacitance of 110 F/g (in relation to one electrode) in 1 M Na_2SO_4, which is lower than what we obtained for the best-performing NovoCarb beads (i.e., 88% PNC_{1h} with an average bead diameter of 255 nm).[10]

The stability of the NovoCarb is shown in Figure 3E,F for the aqueous and organic electrolytes. Voltage floating is a more demanding benchmarking to survey the electrochemical performance stability compared to voltage cycling.[62] For the aqueous system, a very high electrochemical performance stability was observed with a decrease in capacitance between 6 and 13% after floating at 1.2 V for 100 h. As such, the values stayed above the industry-relevant level of 80% of the initial capacitance.[62] Yet, a significantly higher loss of capacitive energy storage is observed in organic media. Albeit having a vanishing small capacitance of 1 F/g, the nonactivated material PNC_{0h} showed a fair performance stability with a reduction of 27% after 100 h at 2.7 V. Interestingly, $PNC_{0.25h}$ exhibited a drastic performance drop of 90% after 100 h at 2.7 V, while the $PNC_{0.5h}$ maintained 67% of the initial capacitance. The introduction of carbon heteroatoms and active surface sites may have severely reduced the energy storage stability by an enhanced electrolyte degeneration.[63] Longer activation times led to a significantly improved performance stability with capacitive retention between 75 and 85% after 100 h at 2.7 V. Seemingly, the enhanced structural ordering of the carbon and removal of more disordered material as seen from Raman analysis (Supporting Information Figure S6) leads to an improved energy storage capacity retention.

DOI: 10.1021/acsami.6b00669
ACS Appl. Mater. Interfaces 2016, 8, 9104−9115

3.4. Electrochemical Performance in an Aqueous Redox Electrolyte. Since the NovoCarb beads exhibit a very high total pore volume with a large fraction of micropores and the potential for facile ion transport, the material is highly attractive for use with redox electrolytes. Besides the pore volume, a highly concentrated redox electrolyte is expected to be advantageous for maximizing redox activity and accomplishing high ion conductivities.[64,65] So far, potassium iodide (KI) had only been explored up to 1 M concentration, yet the low concentrated KI systems have shown already promising performances such as high cyclic lifetime, high energy density, and power density via the variety of halide oxidation states and possibly no need of ion selective membrane through the specific adsorption of the oxidized halide into carbon micropores.[28] The solubility of the KI aqueous solution is very high as compared to other redox electrolyte solutions such as vanadyl sulfate (<3.5 M), potassium ferricyanide (<1.2 M), or hydroquinone solutions (<1 M) at room temperature.[66] For that reason, we provide first data for the potassium iodide system at 6 M concentration and benchmark the performance of PNC_{2h} (i.e., the sample with the largest pore volume) in comparison with conventional AC.

In our experiments, we were able to charge the cells using aqueous KI safely up to 1.4 V cell voltage. Extended *S*-value testing surveyed the entire range of cell voltages up to 1.4 V for the 6 M KI system in AC and PNC_{2h} (Figure 4C). *S*-value testing indicates the onset of enhanced charge transfer related to nonreversible reactions, and values below 0.1 are deemed indicative of stable cell performance.[62] Within the studied range for both molar concentrations of potassium iodide, the second derivative of *S*-values remained below 0.05.

The increase in energy storage capacity at higher concentration can be seen from the galvanostatic charge/discharge profiles in Figure 4A for AC when transitioning from 1 M potassium iodide to 6 M KI. By deriving the specific energy by adequately considering the noncapacitive energy storage mechanism and noncapacitive GCPL shape following the procedure outlined in ref 67 and using eq 3, we calculate for the 1 M KI system in AC a maximum value of 18.4 W·h/kg at a low specific power of 36 W/kg. Note that due to the noncapacitive and nonpseudocapacitive response of the system, values for the specific capacitance (i.e., F/g) are disfavored to avoid misleading data and values are just given for the specific energy. For comparison, 6 M KI yielded at 40 W/kg a maximum specific energy of 22.0 W·h/kg in AC. This performance was severely surpassed when using PNC_{2h} and a specific energy of 29.5 W·h/kg was obtained at 33 W/kg for 6 M KI. This corresponds with a Coulombic efficiency of 98% and an energy efficiency of 74%. For comparison, Laheäär et al. recently reported for a system employing 0.5 M KI and operating at 1.6 V an energy efficiency of 52% and a Coulombic efficiency of 91% (86% and 97%, respectively, at 1.2 V).[67] At even lower specific power (i.e., 17 W/kg), a value of 32.6 W·h/kg was calculated for PNC_{2h} in 6 M KI at 1.4 V, and at a high specific power of 5.7 kW/kg, the system still provided a performance of 13.3 W·h/kg. The PNC_{2h} electrode with 6 M KI maintained about 4.6 W·h/kg at a very high specific power of 12.3 kW/kg. It seems that the system does not show a complete diffusion limited feature of the iodine redox reactions. The high power performance of PNC_{2h} electrode with 6 M KI can be explained by the confinement of redox ions in the micropores which overcome the diffusion limitation through micropores exhibiting pore size smaller than the equivalent diffusion layer.[32] Cyclic stability testing (Figure 4D) showed an excellent stability after 10,000 cycles (virtually no loss in energy storage capacity). The specific energy increased slightly by 4% after 10,000 cycles, due to improved wettability of carbon in aqueous electrolytes after an initial run-in period (conditioning).[4]

3.5. Ragone Plot for Novolac-Derived Carbon Electrodes. The energy vs power performance of the two high energy electrolytes, namely, 1 M TEA-BF_4 in PC (high energy by virtue of the high cell voltage) and aqueous 6 M KI (high energy by virtue of the redox energy storage) is shown for PNC_{2h} and AC (Figure 5). The resulting Ragone chart shows

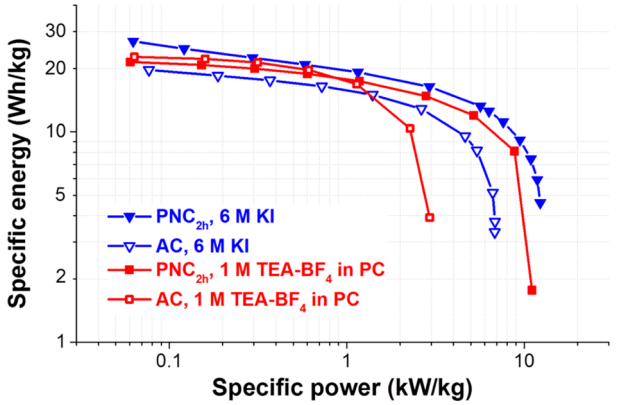

Figure 5. Ragone plot of PNC_{2h} and standard AC with an organic (1 M TEA-BF_4 in PC) and a redox electrolyte (aqueous 6 M KI).

the high potential of novolac-derived carbon beads for electrochemical energy storage, constantly yielding higher power handling and, at the same specific power, higher specific energy when compared to a common activated carbon (Table 5). The zeolite-templated carbons (ZTC) have a SSA similar to that of NovoCarb but have a higher specific capacitance, due to ordered structure and narrow PSD of the ZTCs which makes the pores well-accessible.[68] The main disadvantage of ZTC is the complex synthesis which requires toxic reactants (furfuryl alcohol or acetonitrile) and hydrofluoric acid. The AC, BP2000, activated carbon aerogel, biowaste-derived carbon, and onion-like carbon (OLC) show a lower capacitance than PNC_{2h} due to their lower SSAs. The rate handling behavior of the PNC_{2h} is quite similar to OLC, which is known for its good conductivity which makes it a promising material as a conductive additive.[61] The high rate performance of NovoCarb makes the use of conductive additives redundant. The relative performance of BP2000 at high rates is best, but the specific capacitance of the NovoCarb is still higher. The beneficial performance is particularly attractive when considering the very low raw material costs of the novolac precursor of currently around 3 €/kg (as specified by the manufacturer) and the simple synthesis procedure.

4. CONCLUSIONS

Our work presents a facile synthesis method to obtain ultrasmall spherical carbon particles with a high specific surface and pore volume. A key advantage of our synthesis route is the facile self-emulsifying feature of the novolac−ethanol−water mixture. Therefore, no high shearing forces are needed to produce particles with an average diameter of 300 nm, setting this process apart from the established MAST carbon process.

DOI: 10.1021/acsami.6b00669
ACS Appl. Mater. Interfaces 2016, 8, 9104−9115

Table 5. Overview of the Electrochemical Performance of NovoCarb-Material Compared to Other Carbon Materials for Supercapacitor Applications in Organic Media[a]

material	ref	SSA_{BET} (m^2/g)	electrolyte	specific capacitance at 0.1 A/g (F/g)	capacitance loss at 10 A/g (%)
PNC_{2h}	this work	3104	1 M TEA-BF_4 in PC	123	29
zeolite-templated carbon	68	3040	1 M TEA-BF_4 in PC	168	*not reported*
activated carbon (YP-80, Kuraray)	this work	2347	1 M TEA-BF_4 in PC	103	48
biowaste-derived carbon	69	1635	1 M TEA-BF_4 in PC	75	*not reported*
activated carbon aerogel	70	1408	1 M TEA-BF_4 in PC	101	*not reported*
activated carbon black (BP2000)	61	1389	1 M TEA-BF_4 in PC	90	18
activated carbon black (BP2000	61	1389	1 M TEA-BF_4 in ACN	86	9
carbon onions	61	398	1 M TEA-BF_4 in PC	18	28
carbon onions	61	398	1 M TEA-BF_4 in ACN	18	10

[a]The data are arranged by descending BET surface area.

Pyrolyzed material already exhibits a SSA_{DFT} of 771 m^2/g with a total pore volume of 0.26 cm^3/g due to ethanol acting as a pore former. The sub-micrometer spheres are ideal for a physical activation which can further increase the SSA_{DFT} to 2237 m^2/g (total pore volume, 1.71 cm^3/g).

The specific capacitance of the novolac-derived carbon beads can reach approximately 125 F/g in an aqueous or organic electrolyte. The materials showed excellent performance at high scan rates and current densities with capacitance retention of approximately 80% at 50 A/g in aqueous and approximately 30% at 50 A/g in (highly viscous) organic electrolyte. For the redox electrolyte system, the combination of high molar concentration of potassium iodide (i.e., 6 M) and the large pore volume of PNC_{2h} enabled a very high specific energy exceeding 30 W·h/kg. Thereby, it is possible with an aqueous redox electrolyte to reach energy densities similar to that of an organic electrolyte. Due to the adjustability of the porosity via physical activation, novolac-derived carbon beads are highly promising for not only electrochemical energy storage but also for capacitive deionization as well as flow capacitor applications where spherical particles are preferable for the low viscosity.

■ ASSOCIATED CONTENT

Supporting Information

The Supporting Information is available free of charge on the ACS Publications website at DOI: 10.1021/acsami.6b00669.

Electrode properties, reaction scheme, cell setup, scanning and transmission electron micrographs, combined thermogravimetry with mass spectroscopy data, Raman spectra, skeletal density, elemental analysis, and supplementary electrochemical data (PDF)

■ AUTHOR INFORMATION

Corresponding Author

*E-mail: volker.presser@leibniz-inm.de.

Notes

The authors declare no competing financial interest.

■ ACKNOWLEDGMENTS

We acknowledge funding from the German Federal Ministry for research and Education (BMBF) in support of the nanoEES^{3D} project (Award No. 03EK3013) as part of the strategic funding initiative energy storage framework. We kindly acknowledge the continuing support of Prof. Eduard Arzt (INM). Furthermore, we thank Ralph Schäfer from Allnex Germany GmbH for his help and supply of ALVONOL PN 320. We thank Karl-Peter Schmitt for his support with the hydrothermal process, Robert Drumm for the TGA-MS measurements, Andrea Jung for the CHNS analysis, and Daekyu Kim for the cell assembly (all at INM). This work was supported by the CREATe-Network Project, Horizon 2020 of the European Commission (RISE Project No. 644013). We also thank Dr. Daniel Weingarth, Anna Schreiber, and Marco Zeiger (all at the INM) for helpful discussions and their kind support.

■ REFERENCES

(1) Beguin, F., Frackowiak, E., Eds. *Supercapacitors: Materials, Systems and Applications*. Wiley-VCH Verlag: Weinheim, Germany, 2013; 568 pp.

(2) Simon, P.; Gogotsi, Y. Materials for Electrochemical Capacitors. *Nat. Mater.* **2008**, *7*, 845−854.

(3) Ibrahim, H.; Ilinca, A.; Perron, J. Energy Storage Systems—Characteristics and Comparisons. *Renewable Sustainable Energy Rev.* **2008**, *12* (5), 1221−1250.

(4) Aslan, M.; Weingarth, D.; Jäckel, N.; Atchison, J. S.; Grobelsek, I.; Presser, V. Polyvinylpyrrolidone as Binder for Castable Supercapacitor Electrodes with High Electrochemical Performance in Organic Electrolytes. *J. Power Sources* **2014**, *266*, 374−383.

(5) Inagaki, M.; Konno, H.; Tanaike, O. Carbon Materials for Electrochemical Capacitors. *J. Power Sources* **2010**, *195* (24), 7880−7903.

(6) Zang, L.; Cao, X.; Zhang, Y.; Sun, L.; Qin, C.; Wang, C. Microfluidic Generation of Graphene Beads for Supercapacitor Electrode Materials. *J. Mater. Chem. A* **2015**, *3*, 22088−22093.

(7) Tang, K.; Fu, L.; White, R. J.; Yu, L.; Titirici, M.-M.; Antonietti, M.; Maier, J. Hollow Carbon Nanospheres with Superior Rate Capability for Sodium-Based Batteries. *Adv. Energy Mater.* **2012**, *2* (7), 873−877.

(8) Pérez, C. R.; Yeon, S.-H.; Ségalini, J.; Presser, V.; Taberna, P.-L.; Simon, P.; Gogotsi, Y. Structure and Electrochemical Performance of Carbide-Derived Carbon Nanopowders. *Adv. Funct. Mater.* **2013**, *23* (8), 1081−1089.

(9) Rose, M.; Korenblit, Y.; Kockrick, E.; Borchardt, L.; Oschatz, M.; Kaskel, S.; Yushin, G. Hierarchical Micro- and Mesoporous Carbide-Derived Carbon as a High-Performance Electrode Material in Supercapacitors. *Small* **2011**, *7* (8), 1108−1117.

(10) Oschatz, M.; Zeiger, M.; Jäckel, N.; Strubel, P.; Borchardt, L.; Reinhold, R.; Nickel, W.; Eckert, J.; Presser, V.; Kaskel, S. Emulsion Soft Templating of Carbide-Derived Carbon Nanospheres with Controllable Porosity for Capacitive Electrochemical Energy Storage. *J. Mater. Chem. A* **2015**, *3*, 17983−17990.

(11) Kalpana, D.; Karthikeyan, K.; Renganathan, N. G.; Lee, Y. S. Camphoric Carbon Nanobeads − A New Electrode Material for Supercapacitors. *Electrochem. Commun.* **2008**, *10* (7), 977−979.

DOI: 10.1021/acsami.6b00669
ACS Appl. Mater. Interfaces 2016, 8, 9104−9115

(12) Sharon, M.; Mukhopadhyay, K.; Yase, K.; Iijima, S.; Ando, Y.; Zhao, X. Spongy Carbon Nanobeads—A New Material. *Carbon* **1998**, *36* (5−6), 507−511.
(13) Landfester, K. Miniemulsion Polymerization and the Structure of Polymer and Hybrid Nanoparticles. *Angew. Chem., Int. Ed.* **2009**, *48* (25), 4488−4507.
(14) Sanchez-Dominguez, M.; Aubery, C.; Solans, C., New Trends on the Synthesis of Inorganic Nanoparticles Using Microemulsions as Confined Reaction Media. In *Smart Nanoparticles Technology*, Hashim, A., Ed.; InTech Europe: Rijeka, Croatia, 2012; Chapter 9, pp 195−220, DOI: 10.5772/33010.
(15) Yang, J.-B.; Ling, L.-C.; Liu, L.; Kang, F.-Y.; Huang, Z.-H.; Wu, H. Preparation and Properties of Phenolic Resin-Based Activated Carbon Spheres with Controlled Pore Size Distribution. *Carbon* **2002**, *40*, 911−916.
(16) Singh, A.; Lal, D. Microporous Activated Carbon Spheres Prepared from Resole-Type Crosslinked Phenolic Beads by Physical Activation. *J. Appl. Polym. Sci.* **2008**, *110* (5), 3283−3291.
(17) Fang, Y.; Gu, D.; Zou, Y.; Wu, Z.; Li, F.; Che, R.; Deng, Y.; Tu, B.; Zhao, D. A Low-Concentration Hydrothermal Synthesis of Biocompatible Ordered Mesoporous Carbon Nanospheres with Tunable and Uniform Size. *Angew. Chem., Int. Ed.* **2010**, *49* (43), 7987−7991.
(18) Huang, Y.-P.; Hsi, H.-C.; Liu, S.-C. Preparation of Spherical Activated Phenol-Formaldehyde Beads from Bamboo Tar for Adsorption of Toluene. *J. Air Waste Manage. Assoc.* **2013**, *63* (8), 977−983.
(19) Slomkowski, S.; Alemán, J. V.; Gilbert, R. G.; Hess, M.; Horie, K.; Jones, R. G.; Kubisa, P.; Meisel, I.; Mormann, W.; Penczek, S.; Stepto, R. F. T. Terminology of Polymers and Polymerization Processes in Dispersed Systems (IUPAC Recommendations 2011). *Pure Appl. Chem.* **2011**, *83* (12), 2229−2259.
(20) Wan, J.; Wang, S.; Li, C.; Zhou, D.; Chen, J.; Liu, Z.; Yu, L.; Fan, H.; Li, B.-G. Effect of Molecular Weight and Molecular Weight Distribution on Cure Reaction of Novolac with Hexamethylenetetramine and Properties of Related Composites. *Thermochim. Acta* **2012**, *530*, 32−41.
(21) Ahmadpour, A.; Do, D. D. The Preparation of Active Carbons from Coal by Chemical and Physical Activation. *Carbon* **1996**, *34* (4), 471−479.
(22) Bleda-Martínez, M. J.; Maciá-Agulló, J. A.; Lozano-Castelló, D.; Morallón, E.; Cazorla-Amorós, D.; Linares-Solano, A. Role of Surface Chemistry on Electric Double Layer Capacitance of Carbon Materials. *Carbon* **2005**, *43* (13), 2677−2684.
(23) Maciá-Agulló, J. A.; Moore, B. C.; Cazorla-Amorós, D.; Linares-Solano, A. Activation of Coal Tar Pitch Carbon Fibres: Physical Activation vs. Chemical Activation. *Carbon* **2004**, *42* (7), 1367−1370.
(24) Tennison, S. R. Phenolic-Resin-Derived Activated Carbons. *Appl. Catal., A* **1998**, *173* (2), 289−311.
(25) Tennison, S. R.; Kozynchenko, O. P.; Strelko, V. V.; Blackburn, A. J. Porous Carbons. U.S. Patent US 20040024074 A1, 2008
(26) Fernández, J. A.; Tennison, S.; Kozynchenko, O.; Rubiera, F.; Stoeckli, F.; Centeno, T. A. Effect of Mesoporosity on Specific Capacitance of Carbons. *Carbon* **2009**, *47* (6), 1598−1604.
(27) Frackowiak, E.; Meller, M.; Menzel, J.; Gastol, D.; Fic, K. Redox-Active Electrolyte for Supercapacitor Application. *Faraday Discuss.* **2014**, *172*, 179−198.
(28) Frackowiak, E.; Fic, K.; Meller, M.; Lota, G. Electrochemistry Serving People and Nature: High-Energy Ecocapacitors based on Redox-Active Electrolytes. *ChemSusChem* **2012**, *5* (7), 1181−1185.
(29) Akinwolemiwa, B.; Peng, C.; Chen, G. Z. Redox Electrolytes in Supercapacitors. *J. Electrochem. Soc.* **2015**, *162* (5), A5054−A5059.
(30) Roldán, S.; Granda, M.; Menendez, R.; Santamaria, R.; Blanco, C. Mechanisms of Energy Storage in Carbon-Based Supercapacitors Modified with a Quinoid Redox-Active Electrolyte. *J. Phys. Chem. C* **2011**, *115* (35), 17606−17611.
(31) Roldán, S.; Blanco, C.; Granda, M.; Menéndez, R.; Santamaría, R. Towards a Further Generation of High-Energy Carbon-Based Capacitors by Using Redox-Active Electrolytes. *Angew. Chem.* **2011**, *123* (7), 1737−1739.
(32) Narayanan, R.; Bandaru, P. R. High Rate Capacity through Redox Electrolytes Confined in Macroporous Electrodes. *J. Electrochem. Soc.* **2015**, *162* (1), A86−A91.
(33) Schneider, C. A.; Rasband, W. S.; Eliceiri, K. W. NIH Image to ImageJ: 25 years of Image Analysis. *Nat. Methods* **2012**, *9* (7), 671−675.
(34) Presser, V.; McDonough, J.; Yeon, S.-H.; Gogotsi, Y. Effect of Pore Size on Carbon Dioxide Sorption by Carbide Derived Carbon. *Energy Environ. Sci.* **2011**, *4* (8), 3059.
(35) Vishnyakov, A.; Ravikovitch, P. I.; Neimark, A. V. Molecular Level Models for CO_2 Sorption in Nanopores. *Langmuir* **1999**, *15* (25), 8736−8742.
(36) Gor, G. Y.; Thommes, M.; Cychosz, K. A.; Neimark, A. V. Quenched Solid Density Functional Theory Method for Characterization of Mesoporous Carbons by Nitrogen Adsorption. *Carbon* **2012**, *50* (4), 1583−1590.
(37) Brunauer, S.; Emmett, P. H.; Teller, E. Adsorption of Gases in Multimolecular Layers. *J. Am. Chem. Soc.* **1938**, *60* (2), 309−319.
(38) Presser, V.; McDonough, J.; Yeon, S. H.; Gogotsi, Y. Effect of Pore Size on Carbon Dioxide Sorption by Carbide Derived Carbon. *Energy Environ. Sci.* **2011**, *4* (8), 3059−3066.
(39) Weingarth, D.; Zeiger, M.; Jäckel, N.; Aslan, M.; Feng, G.; Presser, V. Graphitization as a Universal Tool to Tailor the Potential-Dependent Capacitance of Carbon Supercapacitors. *Adv. Energy Mater.* **2014**, *4* (13), 1400316.
(40) Chen, L.; Bai, H.; Huang, Z.; Li, L. Mechanism Investigation and Suppression of Self-Discharge in Active Electrolyte Enhanced Supercapacitors. *Energy Environ. Sci.* **2014**, *7* (5), 1750−1759.
(41) Stoller, M. D.; Ruoff, R. S. Best Practice Methods for Determining an Electrode Material's Performance for Ultracapacitors. *Energy Environ. Sci.* **2010**, *3* (9), 1294−1301.
(42) Trick, K. A.; Saliba, T. E. Mechanisms of the Pyrolysis of Phenolic Resin in a Carbon/Phenolic Composite. *Carbon* **1995**, *33* (11), 1509−1515.
(43) Van der Bruggen, B.; Schaep, J.; Wilms, D.; Vandecasteele, C. Influence of Molecular Size, Polarity and Charge on the Retention of Organic Molecules by Nanofiltration. *J. Membr. Sci.* **1999**, *156* (1), 29.
(44) Zickler, G. A.; Smarsly, B.; Gierlinger, N.; Peterlik, H.; Paris, O. A Reconsideration of the Relationship between the Crystallite Size La of Carbons Determined by X-ray Diffraction and Raman Spectroscopy. *Carbon* **2006**, *44* (15), 3239−3246.
(45) Tuinstra, F.; Koenig, J. L. Raman Spectrum of Graphite. *J. Chem. Phys.* **1970**, *53* (3), 1126−1130.
(46) Ferrari, A. C.; Robertson, J. Interpretation of Raman Spectra of Disordered and Amorphous Carbon. *Phys. Rev. B: Condens. Matter Mater. Phys.* **2000**, *61* (20), 14095.
(47) Faber, K.; Badaczewski, F.; Oschatz, M.; Mondin, G.; Nickel, W.; Kaskel, S.; Smarsly, B. M. In-Depth Investigation of the Carbon Microstructure of Silicon Carbide-Derived Carbons by Wide-Angle X-ray Scattering. *J. Phys. Chem. C* **2014**, *118* (29), 15705−15715.
(48) Ferrari, A. C. A Model To Interpret the Raman Spectry of Disordered Amorphous and Nanostructured Carbons. *MRS Online Proc. Libr.* **2001**, *675*, W11.5.1.
(49) Findeisen, E.; Feidenhans'l, R.; Vigild, M. E.; Clausen, K. N.; Hansen, J. B.; Bentzon, M. D.; Goff, J. P. Hydrogen Concentration and Mass Density of Diamondlike Carbon Films Obtained by X-ray and Neutron Reflectivity. *J. Appl. Phys.* **1994**, *76* (8), 4636.
(50) Béguin, F.; Presser, V.; Balducci, A.; Frackowiak, E. Carbons and Electrolytes for Advanced Supercapacitors. *Adv. Mater.* **2014**, *26* (14), 2219−2251.
(51) Fic, K.; Lota, G.; Meller, M.; Frackowiak, E. Novel Insight into Neutral Medium as Electrolyte for High-Voltage Supercapacitors. *Energy Environ. Sci.* **2012**, *5* (2), 5842−5850.
(52) Barbieri, O.; Hahn, M.; Herzog, A.; Kötz, R. Capacitance Limits of High Surface Area Activated Carbons for Double Layer Capacitors. *Carbon* **2005**, *43* (6), 1303−1310.

DOI: 10.1021/acsami.6b00669
ACS Appl. Mater. Interfaces 2016, 8, 9104−9115

(53) Stoller, M. D.; Magnuson, C. W.; Zhu, Y.; Murali, S.; Suk, J. W.; Piner, R.; Ruoff, R. S. Interfacial Capacitance of Single Layer Graphene. *Energy Environ. Sci.* **2011**, *4* (11), 4685−4689.
(54) Gerischer, H.; McIntyre, R.; Scherson, D.; Storck, W. Density of the Electronic States of Graphite: Derivation from Differential Capacitance Measurements. *J. Phys. Chem.* **1987**, *91* (7), 1930−1935.
(55) Segalini, J.; Iwama, E.; Taberna, P.-L.; Gogotsi, Y.; Simon, P. Steric Effects in Adsorption of Ions from Mixed Electrolytes into Microporous Carbon. *Electrochem. Commun.* **2012**, *15* (1), 63−65.
(56) Yang, C.-M.; Kim, Y.-J.; Endo, M.; Kanoh, H.; Yudasaka, M.; Iijima, S.; Kaneko, K. Nanowindow-Regulated Specific Capacitance of Supercapacitor Electrodes of Single-Wall Carbon Nanohorns. *J. Am. Chem. Soc.* **2007**, *129* (1), 20−21.
(57) Chmiola, J.; Yushin, G.; Gogotsi, Y.; Portet, C.; Simon, P.; Taberna, P. L. Anomalous Increase in Carbon Capacitance at Pore Sizes Less than 1 nm. *Science* **2006**, *313* (5794), 1760−1763.
(58) Chmiola, J.; Largeot, C.; Taberna, P.-L.; Simon, P.; Gogotsi, Y. Desolvation of Ions in Subnanometer Pores and Its Effect on Capacitance and Double-Layer Theory. *Angew. Chem., Int. Ed.* **2008**, *47* (18), 3392−3395.
(59) Raymundo-Piñero, E.; Kierzek, K.; Machnikowski, J.; Béguin, F. Relationship between the Nanoporous Texture of Activated Carbons and Their Capacitance Properties in Different Electrolytes. *Carbon* **2006**, *44* (12), 2498−2507.
(60) Hantel, M. M.; Presser, V.; Kötz, R.; Gogotsi, Y. In Situ Electrochemical Dilatometry of Carbide-Derived Carbons. *Electrochem. Commun.* **2011**, *13* (11), 1221−1224.
(61) Jäckel, N.; Weingarth, D.; Zeiger, M.; Aslan, M.; Grobelsek, I.; Presser, V. Comparison of Carbon Onions and Carbon Blacks As Conductive Additives for Carbon Supercapacitors in Organic Electrolytes. *J. Power Sources* **2014**, *272* (1), 1122−1133.
(62) Weingarth, D.; Noh, H.; Foelske-Schmitz, A.; Wokaun, A.; Kötz, R. A Reliable Determination Method of Stability Limits for Electrochemical Double Layer Capacitors. *Electrochim. Acta* **2013**, *103*, 119−124.
(63) Cericola, D.; Ruch, P. W.; Foelske-Schmitz, A.; Weingarth, D.; Kötz, R. Effect of Water on the Aging of Activated Carbon Based Electrochemical Double Layer Capacitors during Constant Voltage Load Tests. *Int. J. Electrochem. Sci.* **2011**, *6* (4), 988−996.
(64) Wang, W.; Luo, Q.; Li, B.; Wei, X.; Li, L.; Yang, Z. Recent Progress in Redox Flow Battery Research and Development. *Adv. Funct. Mater.* **2013**, *23* (8), 970−986.
(65) Weber, A. Z.; Mench, M. M.; Meyers, J. P.; Ross, P. N.; Gostick, J. T.; Liu, Q. Redox Flow Batteries: A Review. *J. Appl. Electrochem.* **2011**, *41* (10), 1137−1164.
(66) Rahman, F.; Skyllas-Kazacos, M. Solubility of Vanadyl Sulfate in Concentrated Sulfuric Acid Solutions. *J. Power Sources* **1998**, *72* (2), 105−110.
(67) Laheäär, A.; Przygocki, P.; Abbas, Q.; Béguin, F. Appropriate Methods for Evaluating the Efficiency and Capacitive Behavior of Different Types of Supercapacitors. *Electrochem. Commun.* **2015**, *60*, 21−25.
(68) Nishihara, H.; Itoi, H.; Kogure, T.; Hou, P.-X.; Touhara, H.; Okino, F.; Kyotani, F. Investigation of the Ion Storage/Transfer Behavior in an Electrical Double-Layer Capacitor by Using Ordered Microporous Carbons as Model Materials. *Chem. - Eur. J.* **2009**, *15* (21), 5355−5363.
(69) Ramirez-Castro, C.; Schütter, C.; Passerini, S.; Balducci, A. Microporous Carbonaceous Materials Prepared from Biowaste for Supercapacitor Application. *Electrochim. Acta* **2016**, DOI: 10.1016/j.electacta.2015.12.126.
(70) Fang, B.; Wei, Y. Z.; Maruyama, K.; Kumagai, M. High Capacity Supercapacitors Based on Modified Activated Carbon Aerogel. *J. Appl. Electrochem.* **2005**, *35* (3), 229−233.

DOI: 10.1021/acsami.6b00669
ACS Appl. Mater. Interfaces 2016, 8, 9104−9115